

## Electron correlations in an electron bilayer at finite temperature: Landau damping of the acoustic plasmon

This article has been downloaded from IOPscience. Please scroll down to see the full text article.

2000 J. Phys.: Condens. Matter 12 439

(<http://iopscience.iop.org/0953-8984/12/4/306>)

[View the table of contents for this issue](#), or go to the [journal homepage](#) for more

Download details:

IP Address: 171.66.16.218

The article was downloaded on 15/05/2010 at 19:36

Please note that [terms and conditions apply](#).

## Electron correlations in an electron bilayer at finite temperature: Landau damping of the acoustic plasmon

D S Kainth<sup>†</sup>, D Richards<sup>†</sup>, H P Hughes<sup>†</sup>, M Y Simmons<sup>‡</sup> and D A Ritchie<sup>‡</sup>

<sup>†</sup> Optoelectronics Group, Cavendish Laboratory, Madingley Road, Cambridge CB3 OHE, UK

<sup>‡</sup> Semiconductor Physics Group, Cavendish Laboratory, Madingley Road, Cambridge CB3 OHE, UK

Received 1 September 1999

**Abstract.** We report angle-resolved Raman scattering observations of the temperature-dependent Landau damping of the acoustic plasmon in an electron bilayer system realized in a GaAs double-quantum-well structure. Corresponding calculations of the charge-density excitation spectrum of the electron bilayer using forms of the random-phase approximation (RPA), and the static local field formalism of Singwi, Tosi, Land and Sjölander (STLS) extended to incorporate non-zero electron temperature  $T_e$  and phenomenological damping, are also presented. The STLS calculations include details of the temperature dependence of the intra- and inter-layer local field factors and pair correlation functions. Good agreement between experiment and the various theories is obtained for the acoustic plasmon energy and damping for  $T_e \lesssim T_F/2$ , where  $T_F$  is the Fermi temperature. However, contrary to current expectations, all of the calculations show significant departures from our experimental data for  $T_e \gtrsim T_F/2$ . From this, we go on to demonstrate unambiguously that real local field factors fail to provide a physically accurate description of exchange correlation behaviour in low-dimensional electron gases. Our results suggest instead that one must resort to a *dynamical* local field theory, characterized by a *complex* field factor to provide a more accurate description.

### 1. Introduction

Low-dimensional electron gas systems confined in semiconductor heterostructures provide ideal systems for the study of electron–electron interactions, providing a high degree of structural quality and control. The usual theoretical approach adopted for the description of the collective excitation spectra of such systems is the random-phase approximation (RPA). However, the RPA does not include the effects of exchange and correlation, which are expected to be much more important in two-dimensional electron gas (2DEG) systems than in 3D, and to increase in importance as the number density of the system decreases [1]. To account for these effects, many authors have gone beyond the RPA for a description of the excitation spectra of such systems [1–5], by adopting the local field theories of Hubbard [6] and Singwi, Tosi, Land and Sjölander (STLS) [7], which include corrections for exchange and correlation in a simple, physically motivated manner [8, 9]; the success of these approaches can be seen by comparing their results against Monte Carlo calculations [10]. There have also been reports of a number of alternative approaches for including exchange–correlation effects in the excitation spectra of two-dimensional electron systems by adopting:

- (i) a non-local approach within a Hartree–Fock approximation for the evaluation of the irreducible polarizability (see, e.g., references [11] and [12] for the case of inter-subband excitations in quantum wells);

- (ii) alternative static local field approaches such as the quasi-localized charge method [13];
- (iii) a dynamic local field approach within the quantum STLS theory [14].

However, the static local field STLS approach has remained a firm favourite in the published literature. Tests of local field theories for three-dimensional systems have been reported for, e.g., aluminium [15] but there are relatively few reliable experimental tests of these widely used theories in the density range applicable to semiconductor heterostructures. We report here such an experimental test and demonstrate that static local field corrections are unable to provide an accurate description of exchange–correlation behaviour in low-dimensional electron gases. Indeed we will argue that our results point to the need to examine *dynamical* local field theories, embodied by a *complex* local field factor, to achieve a more accurate description of our experimental results.

Electron bilayers (two parallel 2DEGs in close proximity, produced by MBE growth of a GaAs/AlGaAs modulation-doped double-quantum-well heterostructure) have been identified as useful systems for the study of electron correlations in low-dimensional electron systems because the inter-layer Coulomb interaction can effectively counterbalance the kinetic energy of the electrons, allowing many-body effects to dominate. Such a system supports two plasmon modes corresponding to the in-phase (optic plasmon, OP) and out-of-phase (acoustic plasmon, AP) intra-subband oscillations of the charge densities in each layer [16]. Liu *et al* have shown that electron correlations can push the acoustic plasmon curve completely into the single-particle excitation (SPE) spectrum, resulting in Landau damping of the mode at much smaller wavevectors than predicted by the RPA [5]. The acoustic plasmon may therefore be used as a probe of exchange–correlation effects in 2DEG systems, and of Landau damping effects.

Raman spectroscopy is a powerful tool for the study of the electronic excitation spectra of low-dimensional semiconductor systems [17, 18]. For example, measurements of inter-subband excitations in quantum wells have indicated the importance of exchange and correlation in these systems [19]. Applying angle-resolved Raman techniques to electron bilayers, we have recently determined the dispersion of the acoustic plasmon of a double-quantum-well structure [20, 21]. However, the in-plane wavevectors  $q$  accessible ( $q \lesssim 0.15 k_F$  (the Fermi wavevector), for 2DEG areal densities  $N_s \sim 2 \times 10^{11} \text{ cm}^{-2}$ ), determined by the wavelength of the incident light, are too small to probe exchange–correlation corrections to the AP dispersion, as predicted in reference [5]. Attempts to extend the wavevector range by overlaying a grating to couple in higher wavevector transfers [22] did not provide significantly clear results for any conclusions to be drawn; the superposition of the folded AP and OP branches in the reduced Brillouin zone of the grating leads to ambiguities in any analysis of the form of the plasmon dispersions [23]. However, substantial overlap between the SPE continuum and the AP can be obtained by increasing the electron temperature, resulting in the Landau damping of the plasmon, as we have demonstrated recently [20].

In this earlier work we characterized the dependence of the Landau damping of the AP mode in a bilayer system on electron temperature  $T_e$  by comparing the AP peak widths measured using Raman spectroscopy with those calculated using the RPA and the RPA including a Hubbard (static, zero- $T_e$ ) local field correction (H-RPA) to account for exchange–correlation effects [20]. The H-RPA agreed better with the data for low temperatures ( $T_e \lesssim T_F/2$ , where  $T_F$  is the Fermi temperature) than did the RPA, suggesting that exchange–correlation effects are important even for the comparatively high 2DEG densities used; but for higher  $T_e$ , the RPA gave a better fit, suggesting that at higher temperatures ( $T_e \gtrsim T_F/2$ ) exchange–correlation effects become less significant and the RPA the more appropriate approach.

The temperature dependence of the Coulomb drag between two 2DEGs has also been employed recently to study the effects of electron correlations in bilayer systems [24, 25]. The drag mechanism was attributed to Landau damping of the AP [26, 27], but although inclusion

of a 0 K Hubbard local field correction provided a better description of the data than that given by the RPA [24], overall agreement between experiment and theory was not achieved. In both these Raman and Coulomb drag studies [20, 24] it was suggested that using a static local field correction which was  $T_e$ -dependent might be important, and the present work addresses this point in detail by comparing experimental data with corresponding calculations.

We present here Raman scattering measurements of the Landau-damping-induced width of the AP as a function of  $T_e$ , and hence obtain a measure of the overlap of the AP with the SPE continuum and of the importance of exchange and correlation in these systems. The data are modelled using calculations (taking full account of the finite thickness of the quasi-2DEGs, and of phenomenological damping) in:

- (i) the RPA, which is expected to provide a good description when exchange and correlation are not important;
- (ii) the RPA with a 0 K Hubbard local field correction to account for exchange–correlation effects (H-RPA);
- (iii) the self-consistent STLS approach, *modified to include non-zero  $T_e$* .

Most previous theoretical work on exchange–correlation effects in electron bilayers has assumed  $T_e = 0$  K (e.g. references [2] to [5]), but a key feature of our experimental work is that we have raised  $T_e$  substantially ( $\sim T_F$ ), and it is important to account for these observations. The capacity of the STLS approach to include exchange–correlation effects more reliably than the H-RPA at low  $T_e$  is not especially relevant here; indeed, at the relatively high 2DEG densities and momentum range considered here, the RPA and the STLS approach should produce similar results [8]. What is important is that the STLS can be readily modified to account for the effects of non-zero  $T_e$  on the static local field corrections.

As will be shown, there remain discrepancies between our experimental results and those predicted by these theoretical descriptions of electron fluids at non-zero  $T_e$ , and this is one of the central conclusions of this work. In particular, the static STLS and more generally *all* static local field factors fail to describe effectively the effects of exchange and correlation in a non-degenerate 2DEG. However, our results do suggest that a *dynamic* local field correction could provide an effective description.

The theoretical approaches employed are considered in section 2 and appendix A, in which we also provide an overview of the RPA, H-RPA and STLS approximations for electron bilayers. The effects of non-zero temperature and 2DEG thickness on the STLS local field factors and pair correlation functions are considered in section 3. The calculated forms of the lineshapes for Raman scattering from the bilayer plasmons at non-zero temperatures are discussed in section 4. Details of the experimental measurements are provided in section 5 and in section 6 we present the results of our Raman scattering measurements and discuss them in terms of the theoretical models.

## 2. Theory

### 2.1. The RPA for an electron bilayer

Our starting point for a theoretical description of the excitation spectrum of a double-quantum-well system is the RPA, which has been used extensively for the study of the collective excitations in low-dimensional electron systems [28–30], including electron bilayers [16, 31–33]. Throughout, we will be concerned with excitations of angular frequency  $\omega$  and wavevector (parallel to the planes of the 2DEGs)  $q$ . We assume that the two 2DEGs, which will be labelled  $i$  and  $j$ , are isotropic.

The charge-density fluctuation  $\delta\rho_i(q, \omega)$  in layer  $i$  induced by an external potential  $\phi_j^{\text{ext}}(q, \omega)$  in layer  $j$  is given by

$$\delta\rho_i(q, \omega) = \chi_{ij}(q, \omega)\phi_j^{\text{ext}}(q, \omega) \quad (1)$$

where  $\chi_{ij}(q, \omega)$  are the elements of the bilayer density response function  $\bar{\chi}(q, \omega)$ . Within the RPA (and the STLS approximation), this is given by (see reference [4] for further details)

$$\bar{\chi} = \frac{1}{1 - \tilde{v}_{12}\tilde{v}_{21}\chi_1\chi_2} \begin{pmatrix} \chi_1 & \tilde{v}_{12}\chi_1\chi_2 \\ \tilde{v}_{21}\chi_1\chi_2 & \chi_2 \end{pmatrix} \quad (2)$$

where  $\tilde{v}_{ij}(q)$  is an effective interaction between an electron in layer  $i$  and an electron in layer  $j$ ; within the RPA this is the Coulomb interaction  $v_{ij}(q)$ .  $\chi_i(q, \omega)$  is the density response function for a single, isolated layer:

$$\chi_i = \frac{\chi_i^0}{1 - \tilde{v}_{ii}\chi_i^0} \quad (3)$$

where  $\chi_i^0(q, \omega)$  is the 2D Lindhard non-interacting electron polarizability for layer  $i$ .  $\chi^0(q, \omega)$  for a parabolic conduction band is given by [28]

$$\chi^0(q, \omega; \mu, T) = \frac{2m}{\hbar^2} \int \frac{d\mathbf{k}}{(2\pi)^2} \frac{f^0(\mathbf{k} + \mathbf{q}/2) - f^0(\mathbf{k} - \mathbf{q}/2)}{\mathbf{k} \cdot \mathbf{q} - m(\omega + i\gamma)/\hbar} \quad (4)$$

where  $f^0(\mathbf{k})$  is the Fermi-Dirac function for (temperature-dependent) chemical potential  $\mu$  and  $\gamma$  is a phenomenological damping parameter which we take to be the inverse of the single-particle relaxation time ( $\gamma = 1/2\tau_s$ ). Mermin has shown that for non-zero  $\gamma$  the above form for  $\chi^0(q, \omega)$  does not strictly conserve particle number [34]; however, the sample quality in the present work was such that  $\gamma$  was sufficiently small to ensure that the above approximation (equation (4)) is adequate.

To evaluate  $\chi^0(q, \omega)$  for non-zero temperatures we follow the method set out by Maldague [35] and rewrite the integral (equation (4)) as [27]

$$\chi^0(q, \omega; \mu, T) = \int_0^\infty \chi^0(q, \omega; \mu', T = 0) \frac{1}{4k_B T \cosh^2[(\mu - \mu')/(2k_B T)]} d\mu'. \quad (5)$$

The polarizability at zero temperature with non-zero damping is given by [36]

$$\begin{aligned} \chi^0(q, \omega; \mu = E_F, T = 0) &= \frac{2m}{\hbar^2} \frac{k_F}{q} \left[ B\left(-\frac{q}{2k_F} - \frac{\omega}{v_F q} - \frac{i\gamma}{v_F q}\right) - B\left(\frac{q}{2k_F} - \frac{\omega}{v_F q} - \frac{i\gamma}{v_F q}\right) \right] \end{aligned} \quad (6)$$

where

$$\begin{aligned} B(x - i\alpha) &= \frac{1}{\sqrt{2}} \left[ \sqrt{2}x - \text{sgn}(x) \left( (x^2 - \alpha^2 - 1) + \sqrt{(x^2 - \alpha^2 - 1)^2 + 4x^2\alpha^2} \right)^{1/2} \right] \\ &+ \frac{i}{\sqrt{2}} \left[ -\sqrt{2}\alpha + \left( (1 + \alpha^2 - x^2) + \sqrt{(1 + \alpha^2 - x^2)^2 + 4x^2\alpha^2} \right)^{1/2} \right]. \end{aligned} \quad (7)$$

Using equations (6) and (7), equation (5) can be evaluated numerically to give a form for the non-interacting electron polarizability at non-zero temperatures with damping.

For a realistic system, it is also necessary to account for the finite spatial extent of the electron envelope wavefunctions along the confinement direction for the 2DEGs. This is achieved with the Coulomb form factors  $F_{ij}$ , defined by  $F_{ij}(q) = v_{ij}(q)/v(q)$ , where  $v(q) = e^2/2\epsilon\epsilon_0 q$  is the 2D Coulomb interaction and  $\epsilon$  is the effective dielectric function for the media surrounding the bilayer. Interactions between plasmons and phonons were included using a frequency-dependent dielectric constant [21]. Using envelope wavefunctions

$\psi_i(z)$ , determined (for sample structural parameters corresponding to the experimental sample discussed in section 5) from a self-consistent solution of the Poisson and Schrödinger equations (see reference [21] for further details), the form factors

$$F_{ij}(q) = \frac{v_{ij}(q)}{v(q)} = \int dz \int dz' e^{-q|z-z'|} |\psi_i(z)|^2 |\psi_j(z')|^2 \quad (8)$$

were evaluated numerically for wavevectors up to  $q = 6k_F$  and fitted to functions of the forms

$$\begin{aligned} F_{11}(q) &= 1/(1 + bq^m) \\ F_{12}(q) &= \exp(-d^*q^n) \end{aligned} \quad (9)$$

where  $b$ ,  $d^*$ ,  $m$  and  $n$  are fitting parameters. We show in figure 1 the  $q$ -dependence of  $F_{11}$  and  $F_{12}$  determined from equation (8), together with the fits obtained using equation (9). The form factors for the strictly two-dimensional approximation,  $F_{11}^0(q) = 1$  and  $F_{12}^0(q) = \exp(-qd)$ , are also shown for comparison ( $d$  is the effective separation of the 2DEGs [21]); for large wavevector  $q$  the 2D approximations for the form factors fail significantly.

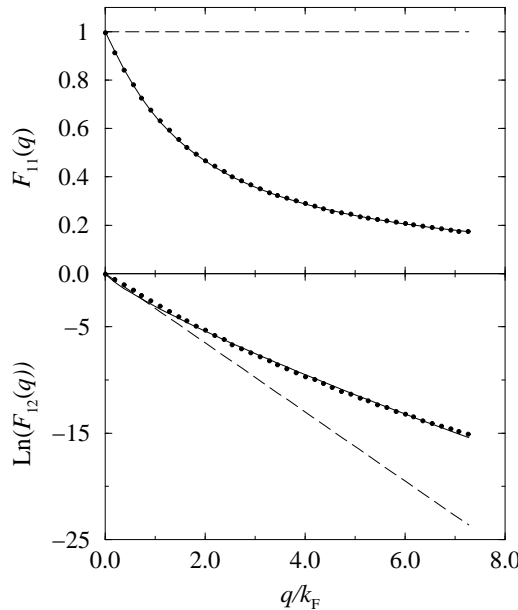


**Figure 1.** The intra-layer and inter-layer Coulomb form factors  $F_{11}$  and  $F_{12}$ , determined with quantum size effects taken into account ( $\bullet$ ). Fits using the functional forms given by equation (9) are indicated by the solid lines. The dashed lines give the form factors  $F_{11}^0(q) = 1$  and  $F_{12}^0(q) = \exp(-qd)$  for the strictly two-dimensional approximation. Note the logarithmic scale for  $F_{12}$ .

The functional forms for the Coulomb form factors given in equation (9), together with  $\chi^0(q, \omega; \mu, T)$  from equation (5), provide  $\chi_i$  (equation (3)) and  $\bar{\chi}(q, \omega; \mu, T)$  (equation (2)) within the RPA.

## 2.2. The optic and acoustic plasmons of an electron bilayer

The energies of the collective charge-density excitations, the plasmons, of the electron bilayer system are given (in the absence of damping,  $\gamma = 0$ ) by the poles of the density response function  $\bar{\chi}(q, \omega)$ . Direct insight into the physical character of the charge-density excitation

spectrum is obtained by diagonalizing  $\bar{\chi}(q, \omega)$ , to give, as the diagonal elements, the density response functions for charge-density fluctuations in which the fluctuations in the two layers are in phase ( $\chi_+$ ) and out of phase ( $\chi_-$ ) [5]:

$$\chi_{\pm} = 2 \left/ \left[ \left( \frac{1}{\chi_1} + \frac{1}{\chi_2} \right) \pm \sqrt{\left( \frac{1}{\chi_1} - \frac{1}{\chi_2} \right)^2 + 4\tilde{v}_{12}^2} \right] \right. \quad (10)$$

The poles of  $\chi_+(q, \omega)$  and  $\chi_-(q, \omega)$  give the optic plasmon (OP) and acoustic plasmon (AP) respectively.

More experimentally realistic response functions, with non-zero damping ( $\gamma \neq 0$ ) allow us to calculate the cross-section  $R(q, \omega)$  for Raman scattering by charge-density fluctuations from the imaginary part of the density response functions [17]:

$$R_{\pm}(q, \omega) \propto -(n(\omega) + 1) \operatorname{Im}[\chi_{\pm}(q, \omega)] \quad (11)$$

and hence the expected Raman lineshapes for the two plasmon modes; the energies of the plasmon modes are determined from the peaks in the intensities  $R_{\pm}(q, \omega)$ . The factor  $(n(\omega) + 1)$  in equation (11), where  $n(\omega)$  is the Bose–Einstein occupation function, was not considered in reference [20], the result of which was to slightly underestimate the asymmetry and widths of the theoretically predicted Raman lineshapes. In this work we will not include this factor in our theoretical analysis but rather correct experimental spectra for its contribution; in particular this allows for a more meaningful comparison between experiment and theory of peak widths, which give a measure of plasmon damping.

### 2.3. The STLS approximation

Although the RPA has been very successful in providing a description of the excitation spectra of 2DEG systems, it takes no account of the effects of exchange and correlation. This failing of the RPA becomes clear if we consider the instantaneous pair correlation functions  $g_{ij}(r)$ , which give the probability of finding an electron at an in-plane position  $r$  in layer  $j$ , given that there is an electron at the origin in layer  $i$  [37]. This is given by [4, 37]

$$g_{ij}(r) = 1 + \frac{1}{\sqrt{N_i N_j}} \int e^{i\mathbf{q} \cdot \mathbf{r}} [S_{ij}(q) - \delta_{ij}] \frac{dq}{(2\pi)^2} \quad (12)$$

where  $N_i$  is the equilibrium number density in layer  $i$ . The static structure factors  $S_{ij}(q)$  are related to the density response function  $\bar{\chi}(q, \omega)$  by the fluctuation-dissipation theorem [38]:

$$S_{ij}(q) = \frac{-\hbar}{2\pi\sqrt{N_i N_j}} \mathcal{P} \int_{-\infty}^{\infty} \coth\left(\frac{\hbar\omega}{2k_B T}\right) \operatorname{Im}[\chi_{ij}(q, \omega)] d\omega \quad (13)$$

where  $\mathcal{P}$  denotes the principal value of the integral.

The RPA gives the unphysical result of negative  $g_{ij}(r)$  for small  $r$ , implying a much deeper exchange–correlation hole than is physically realistic and hence overestimating significantly the correlation energy, the energy of interaction between the electron and its associated correlation hole [4]. To correct for this, Singwi *et al* allowed for a local depletion of the electron density around any given particle [7, 8]. For the two-layer case this *ansatz* leads to an effective interaction between the responding electron in layer  $i$  and the induced charge in layer  $j$  of the form

$$\tilde{v}_{ij}(q) = v_{ij}(q)[1 - G_{ij}(q)] \quad (14)$$

where the local field factors  $G_{ij}(q)$  are given by

$$G_{ij}(q) = \frac{-1}{\sqrt{N_i N_j}} \int \frac{dk}{2\pi^2} \frac{\mathbf{q} \cdot \mathbf{k}}{q^2} \frac{v_{ij}(k)}{v_{ij}(q)} [S_{ij}(|\mathbf{q} - \mathbf{k}|) - \delta_{ij}]. \quad (15)$$

For an electron bilayer system, the  $G_{ij}(q)$  are generally positive and so the inclusion of exchange and correlation creates a ‘hole’ in the induced charge, reducing the strength of the interaction between the responding electron and the induced charge.

From the local field factors  $G_{ij}(q)$  we may determine  $\bar{\chi}(q, \omega)$ , the density response function of the electron bilayer system, using the modified effective potentials  $\tilde{v}_{ij}$  (equation (14)) in equations (2), (3) and (10), which in turn allows a determination of the structure factors  $S_{ij}(q)$  through the fluctuation-dissipation theorem (equation (13)). Thus the determination of the local field factors within the STLS approximation involves the self-consistent evaluation of  $\chi_{ij}(q, \omega)$ ,  $S_{ij}(q)$  and  $G_{ij}(q)$  (equations (2), (13) and (15)).

Our method for the self-consistent evaluation of these STLS local field factors  $G_{ij}$  for a two-layer system at finite temperature is described in detail in appendix A, and mirrors the approaches of Tanaka and Ichimaru, who studied a one-component plasma system at finite temperature in three dimensions within the STLS, principally with a view to modelling stellar cores [38], and of Schweng and Bohm who extended this work to examine a one-component electron liquid in two dimensions [39]. Note that for simplicity we assume that the two layers are of equal density, i.e.  $N_i = N_j = N$ . This approximation is justified for the sample studied experimentally, where any asymmetries between the wells were minimal; calculated Fermi energies for the two wells were within 0.5% and no experimental asymmetries were observed in, e.g., photoluminescence measurements or in the dispersive behaviour of the acoustic and optic plasmon modes at low temperature [20, 21].

The local field factors  $G_{ij}$  evaluated within the self-consistent scheme outlined in appendix A are then used to determine the diagonalized density response functions  $\chi_{\pm}(q, \omega)$  (equation (10)), determined with the Lindhard polarizability given by equations (5) and (6). The RPA result is recovered if the local field factors  $G_{ij}(q)$  are set to zero. These density response functions allow us to determine (through equation (11)), as a function of electron temperature  $T_e$ , the Raman scattering lineshapes for the acoustic and optic plasmons of the electron bilayer, which we then compare with our experimental results.

#### 2.4. The Hubbard approximation—H-RPA

The simplest way to go beyond the RPA is to avoid the self-consistent scheme set out in the previous section and to use instead the Hartree–Fock approximation for the static intra-layer structure factor  $S_{ii}(q)$  [1], which accounts only for the presence of the Pauli hole around each electron at  $T = 0$ . The effects of non-zero temperature and contributions to the local field from intra- and inter-layer Coulomb correlations are therefore neglected in this approximation—the Hubbard correction. The resultant integral for  $G_{ij}(q)$  (equation (15)) can then be evaluated explicitly (within an approximation) to yield [1]

$$G_{ij}^H(q) = \begin{cases} \frac{q}{2\sqrt{q^2 + k_{Fi}^2}} & \text{if } i = j \\ 0 & \text{if } i \neq j \end{cases} \quad (16)$$

where  $k_{Fi}$  is the Fermi wavevector in layer  $i$ .

This Hubbard local field correction  $G_{ij}^H(q)$  was used to account for the effects of electron correlations in the analysis of the Coulomb drag measurements of reference [24] and in our preliminary report on the temperature-dependent Landau damping of the acoustic plasmon in an electron bilayer [20].

### 3. Calculations of correlations in electron bilayers

We present in this section the dependence of the STLS local field corrections  $G_{ij}(q)$  and pair correlation functions  $g_{ij}(r)$  of an electron bilayer on temperature and 2DEG thickness. For all the calculations presented here, we have taken the parameters for the electron bilayer to be those for the sample investigated experimentally (see section 5). In fact the results show that the effects of temperature and non-zero layer thickness on the inter- and intra-layer STLS local field corrections and correlations are not significant for this sample.

#### 3.1. Temperature dependence of local field factors

Our calculations of the temperature-dependent local field factors  $G_{ij}(q)$  for electron bilayers reproduce the results of earlier calculations in the limit of zero temperature and layer thickness. In particular we see similar behaviour of the local field factors, as functions of number density  $N$  (or equivalently  $r_s = (N\pi a_B^2)^{-1/2}$ ) and inter-layer separation ( $d$ ), to that described by Liu *et al* [5].

In figure 2 we show the  $q$ -dependence of the local field corrections  $G_{11}$  and  $G_{12}$  as a function of temperature ( $\theta = T_e/T_F$ ). Although the wavevector range (to  $6 k_F$ ) is not relevant to our experimental work, it was necessary to determine  $G_{ij}$  for large  $q$  in the self-consistent STLS scheme (equation (15)), and we present these results for completeness and to illustrate the integrity of our calculations. The dependence on temperature of  $G_{11}$  and  $G_{12}$  for  $q = 0.2 k_F$  (the typical magnitude of wavevector accessible in the Raman experiments) is illustrated in figure 3. Although  $G_{12}$  increases significantly with temperature, the magnitude of this inter-layer local field factor is negligible for this wavevector.  $G_{11}$ , on the other hand, is much larger

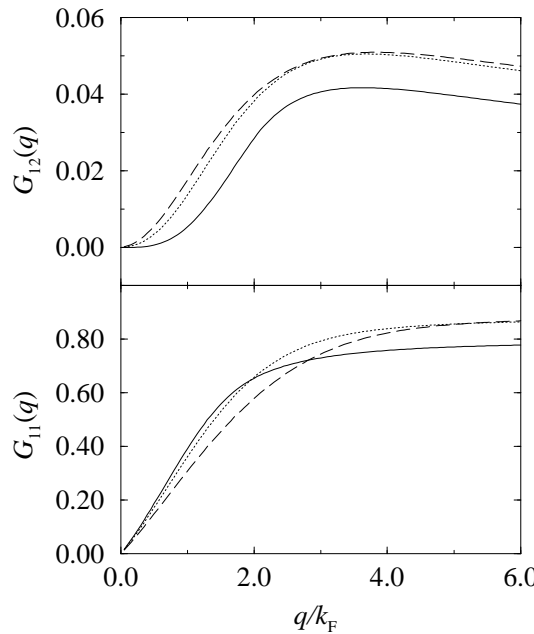


**Figure 2.** Variation of the (a) intra-layer  $G_{11}(q)$  and (b) inter-layer  $G_{12}(q)$  local field factors with wavevector  $q$ , for  $\theta = 0.05$  (solid line), 1.0 (dotted line) and 2.0 (dashed line);  $\theta = T_e/T_F$ ,  $T_F = 78$  K.

and is reduced (although by only  $\sim 5\%$ ) on increasing the temperature from absolute zero to the Fermi temperature.

Figure 4 shows the dependences of  $g_{11}(r)$  and  $g_{12}(r)$ , the pair correlation functions, on  $r$ , for several temperatures; the minimum in the pair correlation functions describes the exchange-correlation hole. The dependence on temperature of the intra-layer pair correlation function  $g_{11}(r)$  is similar to that for a single layer [39]; as  $T_e$  increases, the radius of the exchange-correlation hole is reduced, accompanied by a slight deepening of the hole, in accordance with screening sum rules [37]:

$$\int [1 - g_{ij}(r)] dr = \delta_{ij}. \quad (17)$$

The inter-layer pair correlation function  $g_{12}(r)$  for these comparatively high densities ( $r_s \sim 1.3$ ) is, as expected, close to 1.

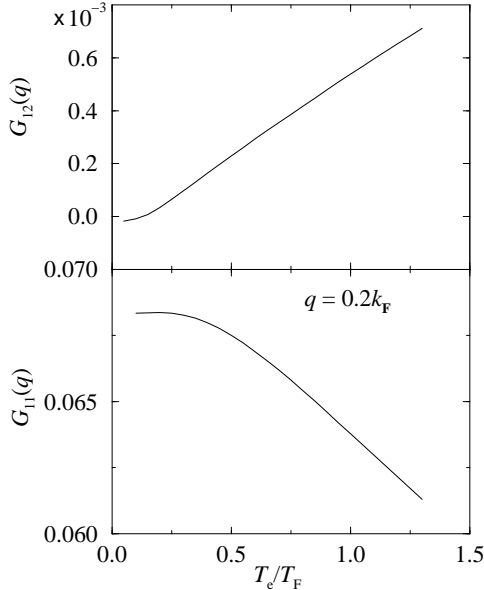


**Figure 3.** Variation of the intra-layer and inter-layer local field factors  $G_{11}(q)$  and  $G_{12}(q)$  with electron temperature  $T_e$ , for  $q = 0.2 k_F$ . Note the scaling factor of  $10^3$  for  $G_{12}$ .

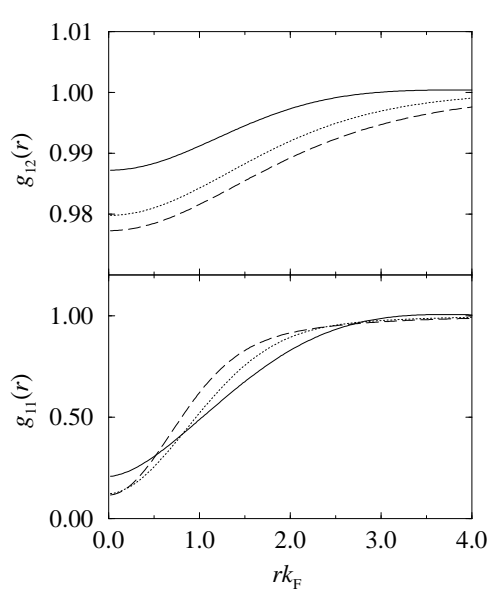


**Figure 4.** Variation of the pair correlation functions  $g_{11}(r)$  and  $g_{12}(r)$ , with in-plane separation  $r$ , for  $\theta = 0.05$  (solid line), 1.0 (dotted line) and 2.0 (dashed line);  $\theta = T_e/T_F$ ,  $T_F = 78$  K.

### 3.2. Quantum size effects

In figure 5 we show the  $q$ -dependence of the intra- and inter-layer local field corrections  $G_{11}$  and  $G_{12}$  determined with the finite-thickness effects of the quantum wells taken into account (using the functional forms for  $F_{11}$  and  $F_{12}$  given in equation (9)), which we compare with the corresponding results determined within the strictly two-dimensional approximation (for which  $F_{11}^0(q) = 1$  and  $F_{12}^0(q) = \exp(-qd)$ ). Our results are in line with those for one-layer systems [1], in that correlations are reduced in going from the ideal to the quasi-2D regime. The greatest discrepancies occur for large wavevector  $q$ , where the 2D approximations for the Coulomb potentials fail significantly (see figure 1). In particular, the inter-layer correlations for a real system do not continue to increase as a function of  $q$ , but instead reach a maximum and then decline.

Figure 6 shows a similar comparison between the quasi-2D and ideal-2D cases for the intra- and inter-layer pair correlation functions,  $g_{11}$  and  $g_{12}$ . Compared with the ideal-2D case, electron-electron effects are expected to be reduced in the quasi-2D regime because the spread of charge in the  $z$ -direction reduces the intra-layer Coulomb interactions; so there should be a shallower intra-layer exchange correlation hole in the quasi-2D regime, as confirmed in the calculations. This shallowing of the intra-layer hole is accompanied by a deepening of the inter-layer hole, as electrons in different layers do not in general want to sit opposite each other. These effects of the charge spreading in the  $z$ -direction are significant for this density ( $r_s \sim 1.3$ ) because the mean distance between the electrons ( $\sim 1/k_F \sim 90 \text{ \AA}$ ) is significantly less than the layer width.

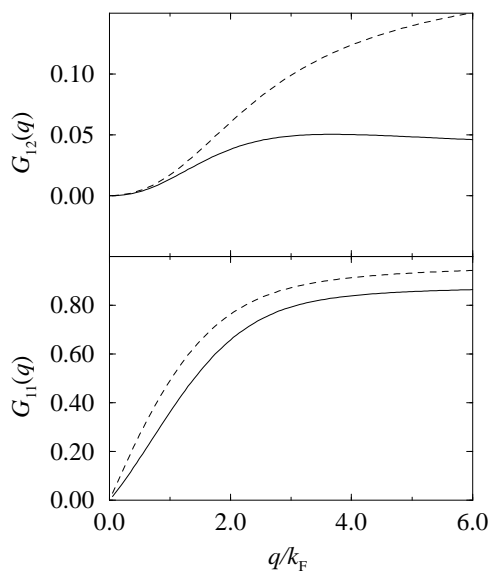


**Figure 5.** A comparison of the  $T = 0$  local field corrections  $G_{11}(q)$  and  $G_{12}(q)$  determined in the ideal-2D approximation (dashed line) and with quantum size effects of the quasi-2DEGs taken into account (solid line).

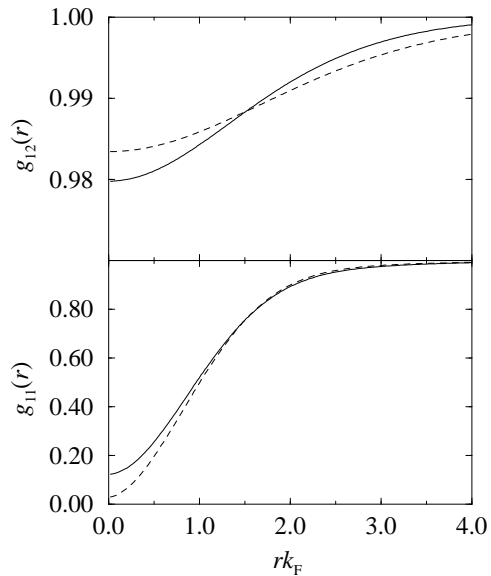


**Figure 6.** The pair correlation functions,  $g_{11}(r)$  and  $g_{12}(r)$ , as for figure 5.

#### 4. Raman scattering from charge-density fluctuations

Figure 7 shows calculated spectra for Raman scattering by the AP (derived from  $-\text{Im}[\chi_-(q, \omega)]$ ), the OP (from  $-\text{Im}[\chi_+(q, \omega)]$ ) and the SPE (from  $-\text{Im}[\chi^0(q, \omega)]$ ) for  $T_e = 10 \text{ K}$  and  $50 \text{ K}$ . As  $T_e$  increases, the SPE spectrum spreads upwards in energy, as expected. This results in an increasing population of electrons travelling with the same velocity as the phase velocity of the AP. These electrons are able to exchange energy efficiently with the plasmon and so enhanced scattering of the AP by SPE occurs, resulting in an asymmetric broadening of the AP peak on the low-energy side, a clear signature of Landau damping [40]. The degree of AP broadening, and its asymmetry, can be characterized (this will be discussed later) in terms of the halfwidths on the higher- and lower-energy sides of the peak. In these calculations the occupation factor ( $n(\omega) + 1$ ) in the Raman intensity (equation (11)) has been omitted, to highlight the effects of Landau damping. The effect of this factor, which becomes more significant with increasing temperature, is to increase the Raman intensity at low Raman

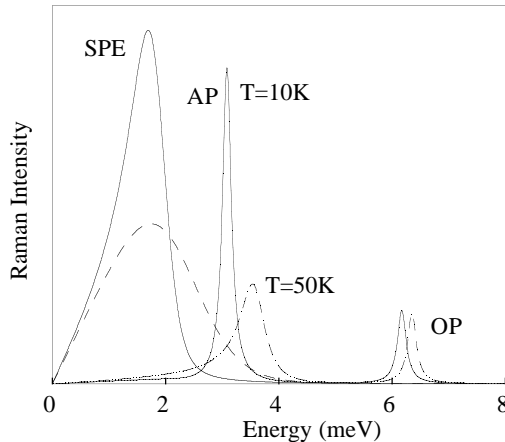


**Figure 7.** Theoretical Raman spectra for charge-density fluctuations and SPE for  $T_e = 10$  K (0.13  $T_F$ —solid line) and  $T_e = 50$  K (0.64  $T_F$ —dashed line). The damping parameter  $\gamma = 0.09$  meV and the wavevector  $q = 1.6 \times 10^5$  cm $^{-1}$ . The occupation factor  $(n(\omega) + 1)$  in equation (11) has been omitted. Peaks due to the acoustic (AP) and optic (OP) plasmons are present in the charge-density-fluctuation spectra. With increasing  $T_e$ , the SPE continuum spreads to higher energies, overlapping the AP energy and leading to an asymmetric broadening of the AP peak, resulting from Landau damping.

shifts, leading to a further slight increase in asymmetry of the AP peak.

Note that the OP peak, at rather higher energy, does not overlap the SPE continuum, and is not detectably broadened by Landau damping, even at 50 K. Figure 7 also shows the upward drift in the energies of the AP and the OP with increasing temperature, a well known classical effect to which we will return.

## 5. Experimental measurements

### 5.1. Sample details

The sample investigated (T229; sample C in references [20] and [21]) consists of two GaAs quantum wells of width  $L_w = 180$  Å, separated by an Al<sub>0.67</sub>Ga<sub>0.33</sub>As barrier of width  $L_b = 125$  Å, giving an effective inter-2DEG separation  $d \sim 305$  Å. These parameters are close to optimal for this study, in that  $L_b$  is large enough to preclude inter-well tunnelling [21] (we have throughout assumed a quantum mechanically decoupled system), while the inter-layer separation  $d$  is small enough to lead to significant inter-layer Coulomb interactions, which depress the energy of the AP mode towards the SPE continuum and increase its susceptibility to many-body effects.

The number densities  $N_1$  and  $N_2$  in the two wells under laser illumination were obtained from a fit, calculated within the STLS approximation, of the low-temperature experimentally determined AP and OP dispersions [21]. It was found that  $N_1$  and  $N_2$  were equal to within  $\sim 5\%$ , as expected since the two wells were grown to be equivalent.  $N_1 = N_2 = (1.95 \pm 0.10) \times 10^{11}$  cm $^{-2}$ ; see reference [21] for further details.

The sample was mounted in a He-cooled cryostat and its temperature controlled by electrical heating.

### 5.2. Determination of the electron temperature

The effect of the 2DEG temperature  $T_e$  on the plasmons was studied by varying  $T_L$ , the lattice temperature. An accurate determination of  $T_e$  was critical for the interpretation of our experiment, and was achieved by carefully studying the quantum well and bulk photoluminescence (PL) lineshapes, determined under the same conditions as the Raman scattering measurements presented below; i.e. for excitation photon energies  $\geq 1.65$  eV and high powers ( $40$  W cm $^{-2}$ ), with  $T_e \geq 25$  K. The strength of the bulk PL signal from the GaAs buffer layer was found to be some 25 times greater than the quantum well signal, as shown in figure 8(a); the lower-energy signal is due to the bulk GaAs, and the weak shoulder at  $\sim 1.53$  eV is the quantum well PL (this assignment has been confirmed by PL and PLE measurements performed with lower power densities and electron temperatures). Consequently the PL tail from the bulk GaAs must be fitted and subtracted from the experimental spectra to give the quantum well PL; a fit to the bulk PL lineshape is shown in figure 8(a).

Having stripped the PL spectrum of the bulk PL, the remaining quantum well PL lineshape  $\mathcal{L}_{\text{QW}}(\omega)$  was taken to be

$$\mathcal{L}_{\text{QW}}(\omega, T_e) \propto \sum_k f_e(E_{e,k}, T_e) f_h(E_{h,k}, T_e) \delta(E'_g + E_{e,k} + E_{h,k} - \hbar\omega) \quad (18)$$

where  $f_{e(h)}$  are the Fermi–Dirac occupation factors for electrons (holes) with kinetic energy  $E_{e,k}$  ( $E_{h,k}$ ) and wavevector  $k$ .  $E'_g$  is the quantum well band-gap and  $\hbar\omega$  is the PL photon energy. Given the temperature range over which the measurements were made, simplifications to the form of  $\mathcal{L}_{\text{QW}}(\omega, T_e)$  (e.g. by making assumptions about the degeneracies of the electrons and holes) were not possible, and the experimental quantum well PL lineshapes were fitted to  $\mathcal{L}_{\text{QW}}(\omega)$  assuming only that:

- (i) Coulomb scattering renders the electron and hole temperatures equal;
- (ii) the total extrinsic electron density ( $1.95 \times 10^{11}$  cm $^{-2}$  for each quantum well) did not change with temperature;
- (iii) the photocreated and thermal electron and hole population densities (used as fitting parameters) were equal.

The electron and hole effective masses were taken to be 0.07 and 0.18 respectively. Note that this procedure cannot quantitatively take into account the effects of disorder which can be important in determining the luminescence lineshape for energies  $E \gg E_F$ . However, for our determination of  $T_e$  we have principally analysed the quantum well PL for energies  $E \lesssim E_F$ .

We show in figure 8(b) a logarithmic plot of the experimental quantum well PL for three different temperatures, along with fits of the form given in equation (18). The data do not fit a straight line (the exponential form often used) except well into the higher-energy part of the PL tails where the errors in the data and disorder effects are significant.

By fitting the bulk and quantum well PL lineshapes in this way, we were able to determine the temperature  $T_e$  of the 2DEG for each Raman measurement with a maximum error (for the highest temperatures) of  $\sim 10\%$ . We were able to derive a value for the lattice temperature  $T_L$  from the form of the variation of  $E_g$  (determined from the bulk PL) with  $T_L$  [41]:

$$E_g = E_g(T_L = 0) - \frac{(5.408 \times 10^{-4} \text{ eV})(T_L/\text{K})^2}{(T_L/\text{K}) + 204}. \quad (19)$$

It was felt that the value determined for  $T_L$  (obtained from a peak energy) had less error associated with it than that for  $T_e$ . We show in the inset of figure 8(a) the variation of  $T_e$  with the lattice temperature  $T_L$ ; the laser illumination is seen to heat the electron gas substantially above the lattice temperature for low  $T_L$  (due to the relatively high photon energy and power

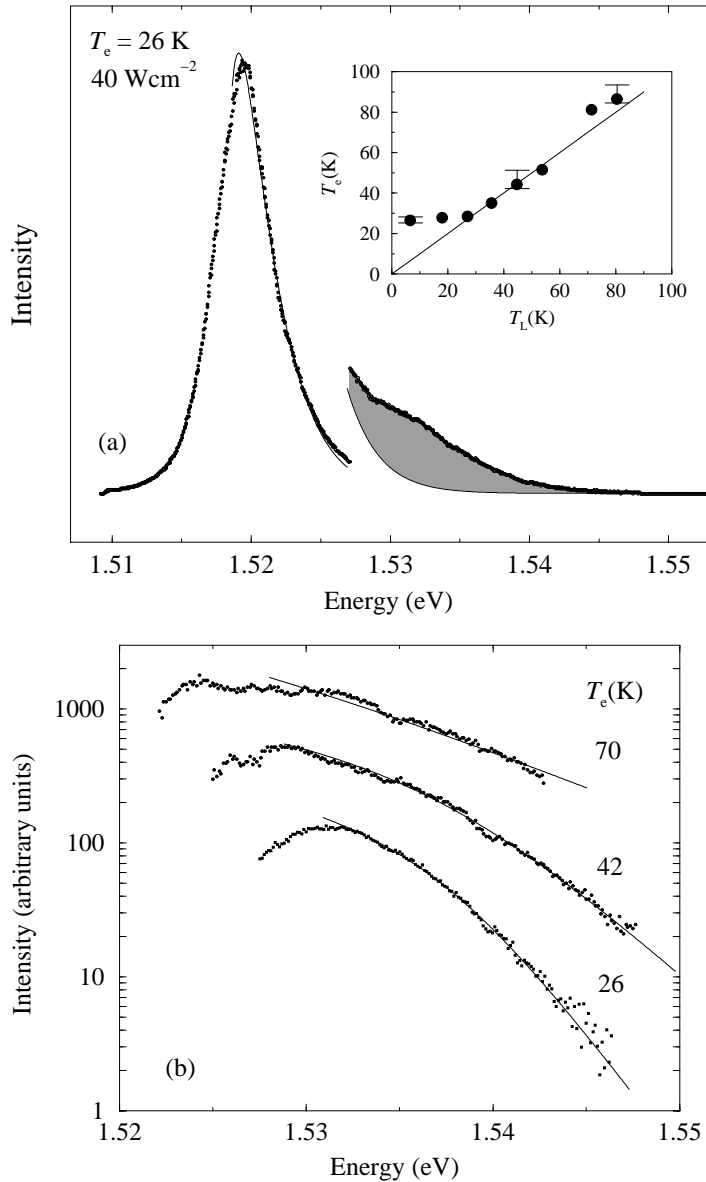


**Figure 8.** (a) The bulk PL signal for  $T_e = 26$  K and a magnified ( $\times 4$ ) view of the quantum well PL. The solid line indicates the fit described in the text. The inset shows the variation of the 2DEG temperature  $T_e$  with the lattice temperature  $T_L$ . (b) The log of the quantum well PL intensity ( $\bullet$ ) for various temperatures  $T_e$  (spectra are displaced vertically for clarity). Fits to the data, using equation (18), are indicated by the solid lines.

densities used), with  $T_e$  and  $T_L$  converging for  $T_L \gtrsim 30$  K. It is important to note that the determinations of  $T_e$  and  $T_L$  are independent; we are able therefore to use the value of  $T_L$  as a lower bound for the value of  $T_e$  (given the heating effects of any incident illumination on the electron gases). Figure 8(a) thus suggests that we do not significantly overestimate the carrier temperature—a factor which has a bearing on the interpretation of our experimental results.

### 5.3. Raman scattering measurements

Angle-resolved Raman scattering measurements were made under incoming resonance conditions, and with the polarizations of the incident and scattered light parallel to allow the observation of plasmons [17]. The band-gap decreased with increasing lattice temperature  $T_L$ , so to maintain the conditions for an incoming resonance the laser wavelength was increased correspondingly. For the low-temperature measurements the energy of the resonance used was 1.656 eV. Rather than determine a resonance profile for each measurement temperature, the shift with increasing  $T_e$  in the resonance energy from this value was determined using  $T_L$  and the known variation of the semiconductor band-gap with temperature (equation (19)).

As the temperature increases, the tail from the bulk band-gap PL increases considerably, and can overwhelm the comparatively weak Raman signals. Fortunately the resonance utilized here was sufficiently far from the band-gap PL to allow Raman measurements to be made over a reasonably large temperature range. The band-gap PL, and the hot PL originating from the inter-band transition responsible for the Raman resonance, limited the Raman measurements to  $T_e \lesssim 110$  K.

### 5.4. Single-particle lifetime

In our calculation of the Raman scattering lineshapes for the plasmon modes, the phenomenological damping constant  $\gamma$  (see equation (4)) is taken to be the inverse of the 2DEG single-particle relaxation time  $\tau_s$ , which we determined experimentally from the dependence of the magnitude of the Shubnikov–de Haas oscillations on the magnetic field; only one Shubnikov–de Haas oscillation frequency was observed, indicating that the two quantum well densities were the same. The amplitude ( $\Delta R$ ) of the Shubnikov–de Haas oscillations is given by [42]

$$\Delta R = 4R_0 X(T) \exp\left(-\frac{\pi}{\omega_c \tau_s}\right) \quad (20)$$

where  $R_0$  is the zero-field resistance,  $\omega_c$  the cyclotron frequency, and  $X(T)$  a thermal damping factor given by

$$X(T) = \frac{2\pi^2 k_B T / \hbar \omega_c}{\sinh(2\pi^2 k_B T / \hbar \omega_c)}. \quad (21)$$

For our samples,  $\tau_s$  was found to be of the order of 3.5 ps for Shubnikov–de Haas oscillations measured at 4 K. Using this value, we were able to fix the low-temperature halfwidth of the plasmons as  $\hbar\gamma = \hbar/2\tau_s = 0.09$  meV.

## 6. Results

### 6.1. Temperature-dependent Raman scattering

A Raman spectrum for  $T_e = 93$  K is shown in figure 9(a); at such high electron temperatures the Raman signals are superimposed on quite intense background PL arising from the quantum well inter-band transition responsible for the Raman resonance ('hot' PL, at small Raman shifts) and also from the GaAs buffer layer (bulk PL, at high Raman shifts). In addition, the importance at such elevated temperatures of the occupation factor in the Raman intensity ( $n(\omega) + 1$  in equation (11)) is also responsible in part for the large intensity at small Raman shifts. In order to facilitate comparison between experiment and theory, especially for the AP damping as characterized by Raman peak widths, the experimental spectra  $I(\omega)$  were first

divided by the occupation factor  $(n(\omega) + 1)$ , as shown in figure 9(a). Fits to the lineshapes  $I(\omega)/(n(\omega) + 1)$  were then obtained using exponential tails to describe the PL contributions to the experimental lineshapes; the result of such a fit is indicated in figure 9(a). The exponential bulk and hot PL tails were then removed to give a corrected Raman signal, also shown in figure 9(a), in which the effect of the occupation factor  $(n(\omega) + 1)$  has been removed.

Figure 9(b) shows Raman spectra measured for a range of electron temperatures  $T_e$ , for an in-plane wavevector transfer  $q = 1.6 \times 10^5 \text{ cm}^{-1}$ . These spectra have been corrected as described above to leave signals due principally to the plasmons. Two peaks are present, which we assign to the acoustic and optic plasmons of the 2DEG [20]. The OP is seen to broaden symmetrically as  $T_e$  rises, whereas the AP is seen to broaden asymmetrically and to a much greater extent.

We ascribe the asymmetric broadening of the AP to Landau damping arising from the increasing interaction with the lower-lying SPE continuum as  $T_e$  is increased (as discussed in section 4 and illustrated in figure 7). The broadening with  $T_e$  of the OP peak may be attributable to increased scattering by un-ionized impurities in the sample bulk as the temperature increases; this scattering is greater for the OP than the AP as away from the bilayer region the electric fields associated with the symmetric OP are much greater than those of the antisymmetric AP [29]. We have also shown that this effect can account for the observed dependence on 2DEG mobility of the relative strengths of Raman scattering by the AP and OP [21].

The observed AP width involves several contributions—Gaussian terms such as inhomogeneous broadening effects, spectrometer resolution and broadening due to the spread of in-plane wavevectors accepted by the numerical aperture of the collecting lens, and Lorentzian contributions from electron scattering (described by the parameter  $\gamma$  in equation (4)) and Landau damping. These combine according to

$$\Delta\omega_L \Delta\omega_{\text{tot}} + (\Delta\omega_G)^2 = \Delta\omega_{\text{tot}}^2 \quad (22)$$

where  $\Delta\omega_L$  ( $\Delta\omega_G$ ) is the Lorentzian (Gaussian) contribution to the total halfwidth at half-maximum (FWHM),  $\Delta\omega_{\text{tot}}$  [43]. To allow easy comparisons with the calculated spectra, the Gaussian contributions to the halfwidths were deconvolved from the experimental spectra by adapting a method originally due to Dobryakov and Lebedev [43]. As a result the net Gaussian contribution to the FWHM (full width at half-maximum) was estimated to be 0.06 meV, in good agreement with the observed width of the Rayleigh scattered laser line (cf. the single-particle relaxation FWHM  $2\gamma = 0.18 \text{ meV}$ ).

Because the AP lineshape is asymmetric, HWHMs on either side were measured and equation (22) used to subtract  $\Delta\omega_G$  in each case to produce  $y_1$  and  $y_2$ , the HWHMs of the Lorentzians on the low- and high-energy sides, respectively (illustrated in figure 9(a)). The width of the AP, once Gaussian contributions have been subtracted, is a measure of the total homogeneous damping experienced by the plasmon mode. The difference between  $y_1$  and  $y_2$ , on the other hand, gives information about the energy-dependent damping responsible for the observed asymmetry of the AP peak; thus  $y_1 - y_2$  gives a direct measure of the Landau damping experienced by the AP. In this way, by comparing  $y_1$  and  $y_2$  with theoretically calculated halfwidths, we have a direct handle on the many-body interactions of the AP with the SPE continuum.

We should note that the SPE band itself is potentially observable in both polarized and depolarized Raman spectra. However, at low temperatures no SPE signal was observed in either polarization for  $q = 1.6 \times 10^5 \text{ cm}^{-1}$ . For  $q = 1.16 \times 10^5 \text{ cm}^{-1}$  the SPE band is in a spectral region too close (a Raman shift less than  $\sim 1 \text{ meV}$ ) to the exciting laser line to be observed.

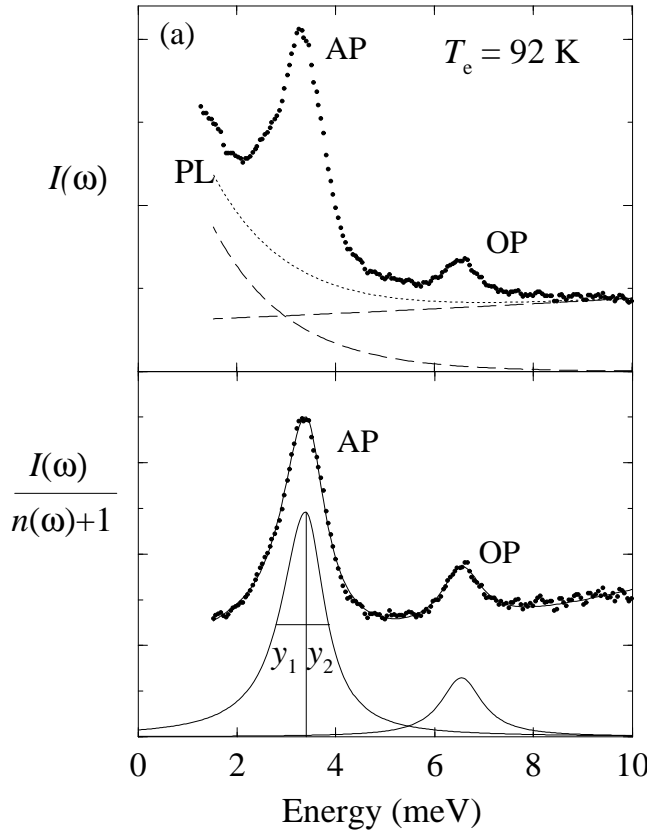


**Figure 9.** (a) A spectrum  $I(\omega)$  measured for an electron temperature  $T_e = 93$  K is shown in the upper panel and the spectrum corrected for the Raman occupation factor  $(n(\omega) + 1)$  is shown in the lower panel;  $q = 1.6 \times 10^5 \text{ cm}^{-1}$ . The points show the experimental spectrum; the solid lines indicate the fit to the spectrum (mainly obscured by the points due to the good fit) and the fit with the exponential backgrounds due to the bulk and hot PL removed. In the upper panel the bulk and hot PL contributions are indicated by the dashed lines, and the total PL contribution by the dotted line. The HWHMs (halfwidths at half-maximum),  $y_1$  and  $y_2$ , used to parametrize the peak widths, are indicated. (b) Corrected Raman spectra (with the background PL spectra subtracted and the  $(n(\omega) + 1)$  occupation factor removed) of the acoustic (AP) and optic (OP) plasmons for various electron temperatures  $T_e$ ;  $q = 1.6 \times 10^5 \text{ cm}^{-1}$ . Note the broadening and developing asymmetry of the AP with increasing  $T_e$ , resulting from Landau damping.

### 6.2. Total AP damping

We now consider the comparison between the experimentally observed and theoretically calculated AP total linewidths as a function of temperature. Figure 10(a) shows a plot of the experimentally determined FWHM ( $y_1 + y_2$ ) for  $q = 1.16 \times 10^5 \text{ cm}^{-1}$ , after removing the Gaussian contributions as described above. The experimental uncertainties in these FWHM values are of the order of  $\pm 0.02$  meV for low  $T_e$ , rising to  $\pm 0.06$  meV for higher temperatures. Figure 10(b) shows the corresponding results for  $q = 1.6 \times 10^5 \text{ cm}^{-1}$ . The three curves show the results of calculations of the FWHM determined within: (i) the RPA; (ii) the H-RPA; (iii) the finite-temperature STLS formalism described in section 2.

We can see from figure 10 that the larger the magnitude of the local field correction  $G_{11}$ , the greater the increase in damping with increasing  $T_e$ ; as the Hubbard intra-layer local field

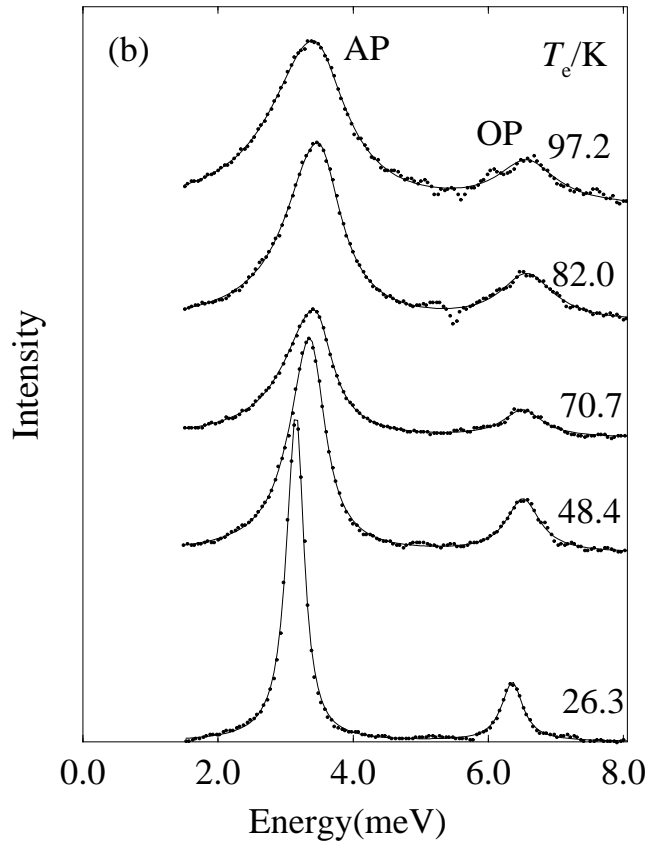


Figure 9. (Continued)

correction  $G_{11}$  is greater than that obtained within the STLS, for a given  $T_e$  the H-RPA predicts a greater width than that calculated using the STLS approximation, which is in turn greater than that obtained within the RPA.

For low  $T_e$ , for both wavevectors, the experimentally determined FWHM and the calculated values agree quite well, especially as it should be noted that no free fit parameters were used for these curves—the 0 K theoretical FWHM was fixed from the experimental single-particle relaxation times (section 5.4). But since the experimental uncertainties at these values of  $T_e$  are smaller than the point size in the figure, the better agreement between the data and the H-RPA and STLS curves, as opposed to the RPA calculation, is significant, and suggests that it is necessary to include exchange–correlation effects even for these densities.

However, the experimentally determined plasmon widths increase with  $T_e$  much more slowly than is predicted theoretically, and for  $T_e \gtrsim T_F$  drop below even the values predicted by the RPA. This could be interpreted in terms of a reduction in the significance of correlation effects at these temperatures, at which the RPA then provides a better description. However, the STLS calculation, which should take full account of the effects of non-zero temperature, does not show this behaviour, reflecting the relative constancy of the intra-layer local field correction  $G_{11}$  over this temperature range (see figure 3). So it appears that for  $T_e \gtrsim T_F$ , further theoretical developments are necessary.

These calculations take no account of any dependence on temperature of the single-particle

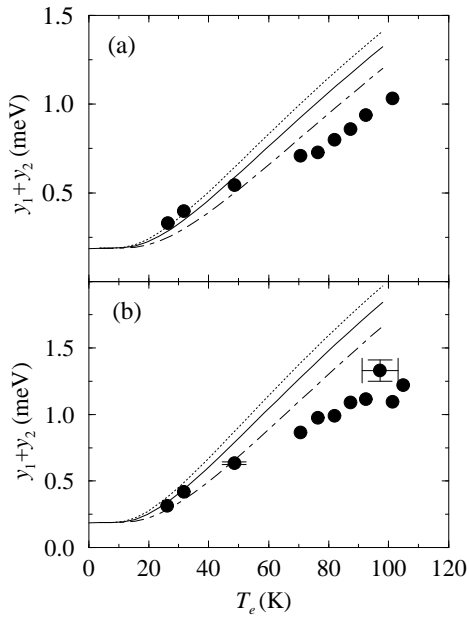


**Figure 10.** Experimental (●) and theoretical (curves) results for the total width of the AP as a function of  $T_e$ . Calculations have been performed within the RPA (dashed line), Hubbard approximation (dotted line) and finite-temperature STLS (solid line). (a)  $q = 1.16 \times 10^5 \text{ cm}^{-1}$ , (b)  $q = 1.6 \times 10^5 \text{ cm}^{-1}$ .

relaxation rate  $\gamma$ . However, if anything we would expect the single-particle lifetime to decrease with increasing temperature, leading to even larger theoretical linewidths than those calculated here and increasing yet further the discrepancy between experiment and theory.

### 6.3. AP asymmetry

For a given  $T_e$  it is expected that the low-energy side of the AP peak will be more affected by Landau damping than the high-energy side, as the SPE continuum lies below the AP dispersion curve. A measure of this asymmetric broadening is  $(y_1 - y_2)$ , which is plotted in figure 11 for both experiment and theory, again for both  $q = 1.16$  and  $1.6 \times 10^5 \text{ cm}^{-1}$ .

It is expected that  $(y_1 - y_2) \rightarrow 0$  as  $T_e \rightarrow 0$  (the peak shape would be a symmetric Lorentzian) and increase with increasing  $T_e$ . Experimentally, for  $q = 1.6 \times 10^5 \text{ cm}^{-1}$  (figure 11(b)),  $(y_1 - y_2)$  increases with low  $T_e$  as expected, but at higher temperatures ( $T_e \sim 70 \text{ K}$ ) it becomes roughly constant. For the smaller wavevector of  $q = 1.16 \times 10^5 \text{ cm}^{-1}$  (figure 11(a)), the discrepancy between experiment and theory is greater and  $(y_1 - y_2)$  is essentially zero over the measured temperature range. In contrast to this, all the theoretical models predict a continuous increase in  $(y_1 - y_2)$  with rising  $T_e$ . It is important to note that any temperature dependence of the single-particle lifetime ( $\sim 1/2\gamma$ ) is unlikely to affect this measure of the asymmetry of the peak; we are sensitive here only to the effects of Landau damping.

Another measure of the Landau damping is provided by the degree of asymmetry,  $\alpha = (y_1 - y_2)/(y_1 + y_2)$ , shown in figure 12 for experiment and for our STLS calculation. For the two wavevectors considered, the STLS theory predicts essentially the same variation with temperature, with  $\alpha$  levelling off near  $T_F$ . This insensitivity of  $\alpha$  to the wavevector is to be expected, as both the AP and the SPE continuum have a similar, approximately

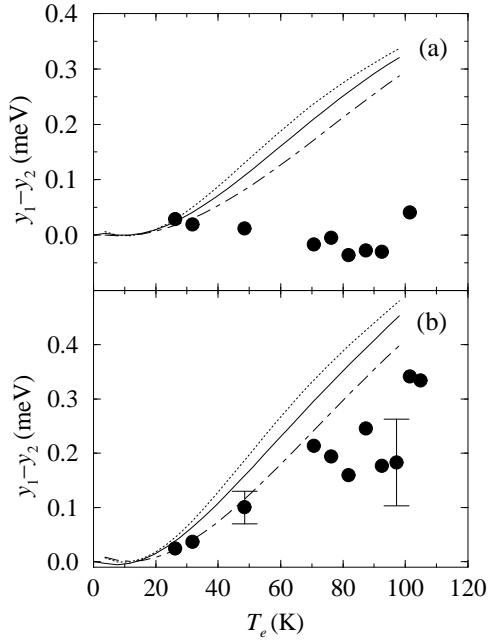


**Figure 11.** The asymmetry of the AP (defined as  $y_1 - y_2$ ), as for figure 10.

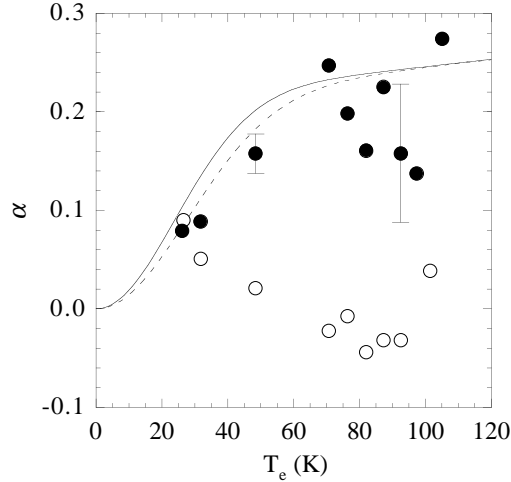


**Figure 12.** The degree of asymmetry of the AP Raman peak,  $\alpha = (y_1 - y_2)/(y_1 + y_2)$ , for experiment (points) and theory, within the finite-temperature STLS formalism (curves), for wavevectors  $q = 1.16$  ( $\circ$ , dashed line) and  $q = 1.6 \times 10^5$   $\text{cm}^{-1}$  ( $\bullet$ , solid line).

linear, dependence on  $q$ , for the small wavevectors ( $q \ll k_F$ ) considered here. However, the experimental results for the two wavevectors are markedly different. For  $q = 1.6 \times 10^5$   $\text{cm}^{-1}$  there is a fairly good agreement between experiment and theory over the whole temperature range, although the experimental uncertainties are large ( $\sim \pm 40\%$  for high  $T_e$ ); note, though, that the calculations overestimate the FWHM of the AP peak at higher temperatures. For  $q = 1.16 \times 10^5$   $\text{cm}^{-1}$  there is a significant discrepancy between experiment and theory.

#### 6.4. AP energy

Figures 13(a) and 13(b) show the energy  $\omega_{AP}$  of the acoustic plasmon as a function of  $T_e$  for  $q = 1.16$  and  $1.6 \times 10^5 \text{ cm}^{-1}$ , for both experiment and theory. The 2DEG density for the calculations was set so that the AP dispersion obtained within the STLS approximation matched the experimentally determined dispersion at low temperature [21]. (Previously [20], the density was obtained using a fit determined within the H-RPA, resulting in a slightly higher density than that used here; this results in the slight shift of the RPA and H-RPA curves with respect to our data for  $(y_1 + y_2)$  (figure 10) and  $(y_1 - y_2)$  (figure 11), compared with those presented in figure 4 of reference [20].)

All the theoretical curves show a large increase ( $\sim 30\%$ ) of the AP energy with temperature, for both wavevectors. The OP energy  $\omega_{OP}$  was also found to increase with  $T_e$ , although by only  $\sim 10\%$ . Such behaviour is well known for classical Maxwell–Boltzmann plasmas [44], and similar calculations carried out for a 2D plasma correspond closely to our RPA results at higher temperatures.

Figure 13 shows that the inclusion of exchange–correlation effects reduces the calculated values of  $\omega_{AP}$ , as would be expected from the softening of the effective interaction potentials  $\tilde{v}_{ij}$  (equation (14)). The weak temperature dependence of the STLS local field correction (see figure 3) does not significantly alter the variation of the plasmon energy with  $T_e$ .

Experimentally, for  $T_e \lesssim 50 \text{ K}$  ( $T_F = 78 \text{ K}$ ),  $\omega_{AP}$  increases with  $T_e$ , in keeping with the calculations. However, for both wavevectors, for  $T_e \gtrsim 50 \text{ K}$ ,  $\omega_{AP}$  remains approximately constant, in contrast with the theories, all of which predict a steady increase in the plasmon energy. The variation of the OP energy  $\omega_{OP}$  with temperature follows essentially the same pattern as that of the AP (see figure 9(b)), although there is better agreement between experiment and theory due to the smaller predicted increase of  $\omega_{OP}$  ( $\sim 10\%$ ) with  $T_e$ .

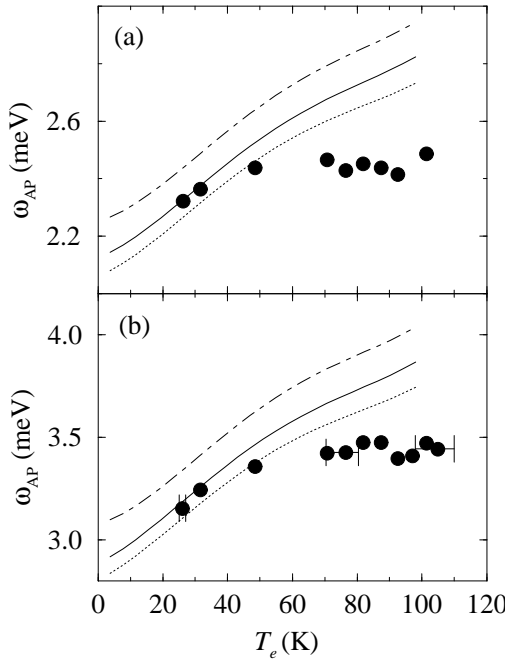
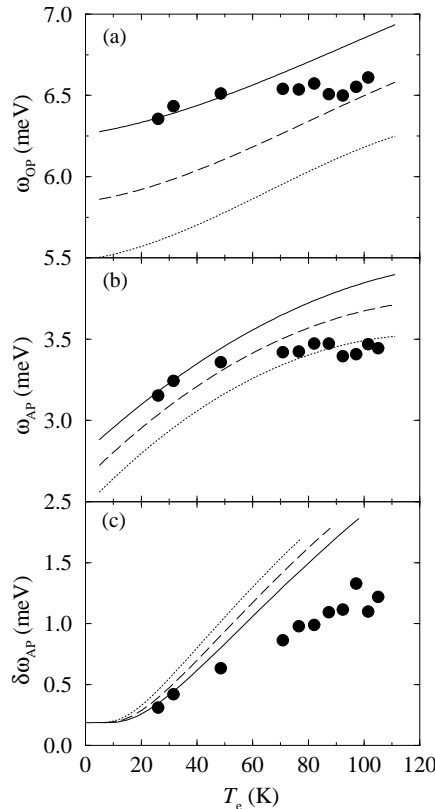


Figure 13. AP energy  $\omega_{AP}$ , as for figure 10.

### 6.5. Discussion

Above  $T_e \sim 50$  K, there are significant discrepancies between experiment and theory. All three calculations show an increase in  $\omega_{AP}$ , contrary to the observed plateau behaviour, and all three overestimate the width and asymmetry. Not only does the RPA fail to describe our results, but so does the full temperature-dependent STLS scheme. We believe that these discrepancies are significant, suggesting a failure of the static local field theories used here to describe adequately the excitation spectra of non-degenerate low-dimensional electron gases.

To demonstrate that this is the case, we must firstly to examine whether alternative causes of the observed plasmon behaviour, such as changes with  $T_e$  of the 2DEG densities, or of their background screening, could explain our experimental results. Figure 14 explores the effect of possible changes in the 2DEG densities by plotting, for various 2DEG densities, calculations of  $\omega_{OP}$ ,  $\omega_{AP}$  and the AP FWHM  $\delta\omega_{AP} \equiv (y_1 + y_2)$  as functions of  $T_e$  for  $q = 1.6 \times 10^5$  cm $^{-1}$ , together with the corresponding experimental results. (For expediency, the STLS local field factors self-consistently determined for a density of  $1.95 \times 10^{11}$  cm $^{-2}$  (figure 3) were used in the calculations for all densities; this can be justified by the small variation in the low  $T_e$ -values for  $G_{11}$  and  $G_{12}$  over the relatively small range of densities considered.) The



**Figure 14.** Experimental (●) and theoretical (curves) temperature ( $T_e$ ) dependences for  $q = 1.6 \times 10^5$  cm $^{-1}$  of (a) the OP energy  $\omega_{OP}$ ; (b) the AP energy  $\omega_{AP}$ ; (c) the AP damping  $\delta\omega_{AP} \equiv (y_1 + y_2)$ . The theoretical curves have been determined for electron densities of (solid lines) 1.95, (dashed lines) 1.7 and (dotted lines)  $1.5 \times 10^{11}$  cm $^{-2}$ , using STLS local field factors given in figure 3.

observed temperature dependence of  $\omega_{AP}$  (figure 14(b)) would require a significant reduction in 2DEG density (by about 30% for the highest measurement temperatures), though a much smaller reduction ( $\sim 15\%$ ) would account for the behaviour of  $\omega_{OP}$  (figure 14(a)). Moreover, figure 14(c) shows that the AP damping  $\delta\omega_{AP}$  actually increases with decreasing density, worsening the discrepancy between experiment and theory; for a given  $T_e$ , the smaller  $T_F$  resulting from a decrease in density effectively increases the reduced temperature  $T_e/T_F$  and enhances the Landau damping. So although a reduction in density with temperature could account for the observed  $T_e$ -dependence of  $\omega_{AP}$ , the corresponding temperature dependence of  $\omega_{OP}$  and  $\delta\omega_{AP}$  cannot be reconciled to this.

We have assumed throughout that the two 2DEGs are of equal density, an assumption borne out at low temperatures from the form of the plasmon dispersions [20, 21]. However, a temperature-induced asymmetry in the electron distribution between the two quantum wells (the total electron density remaining constant) might occur; calculations (within the H-RPA for computational simplicity) show (figure 15(b)) that this would result in a reduction of  $\omega_{AP}$ , and that agreement between experiment and theory is possible at the highest measurement temperatures for  $N_1/N_2 \sim 3$  (i.e.  $N_1 \sim 2.9$  and  $N_2 \sim 1.0 \times 10^{11} \text{ cm}^{-2}$ ). However, not only is this a very significant asymmetry, but again neither the  $T_e$ -dependence of  $\omega_{OP}$ , or that of  $\delta\omega_{AP}$ , fall into line with this. An asymmetric density distribution results in a slight increase in  $\omega_{OP}$  (figure 15(a)) as the two plasmon modes decouple and the OP becomes more localized in the higher-density layer; at the same time the AP becomes more localized in the lower-density layer, leading to the observed reduction in energy. An increasing density asymmetry also leads to an increase in the Landau damping of the AP, which comes closer to (and enters, for a large difference between the densities) the SPE continuum of the higher-density layer [5].

The variations of  $\omega_{OP}$  and  $\omega_{AP}$  with  $T_e$  (see figures 14 and 15) also indicate that changes in background screening (from, e.g., un-ionized donors in the doped AlGaAs layers) are not responsible for the reduction in  $\omega_{AP}$  from the theoretical values. If this were the case, we would expect  $\omega_{OP}$  to be affected to a much greater extent, as seen in the widths of the two plasmon peaks (see section 6.1 and figure 9). In addition, although increased screening would reduce  $\omega_{AP}$ , the SPE continuum would be unaffected, resulting in increased Landau damping, contrary to observation.

It could be argued that agreement between our experimental measurements and calculations could be achieved on the basis that the electron temperature—a quantity, which as we have seen above is relatively difficult to determine—has been overestimated. We have, however, already seen that this explanation is unlikely because  $T_L$ , the lattice temperature (which for temperatures  $\gtrsim 30 \text{ K}$  is almost identical to  $T_e$ ) provides an accurate lower bound for the electron temperature; certainly it is very unlikely that both measures of temperature could overestimate  $T_e$  by  $\sim 35\%$ —the amount required to achieve agreement between the experimental data and the calculations.

Therefore it appears that the inability of our calculations to model our experimental results for the energy and damping of the AP cannot be simply attributed to an experimental artifact, such as a decrease in 2DEG density with temperature. We must thus examine whether the use of a static local field correction provides an accurate description of the effect of exchange and correlation on the excitation spectra of non-degenerate quasi-two-dimensional electron systems. In order to obtain better agreement with experiment for the AP energy, the magnitude of  $G_{11}$  must increase with temperature, whereas to obtain an improved fit for the measured AP damping,  $G_{11}$  must decrease<sup>†</sup>. This contradiction suggests that a real local field factor (as

<sup>†</sup> Changes to the inter-layer local field factor  $G_{12}$  are unlikely to have a significant effect, given the weakness of inter-layer correlations demonstrated in section 3, and so we can set  $G_{12} = 0$ .

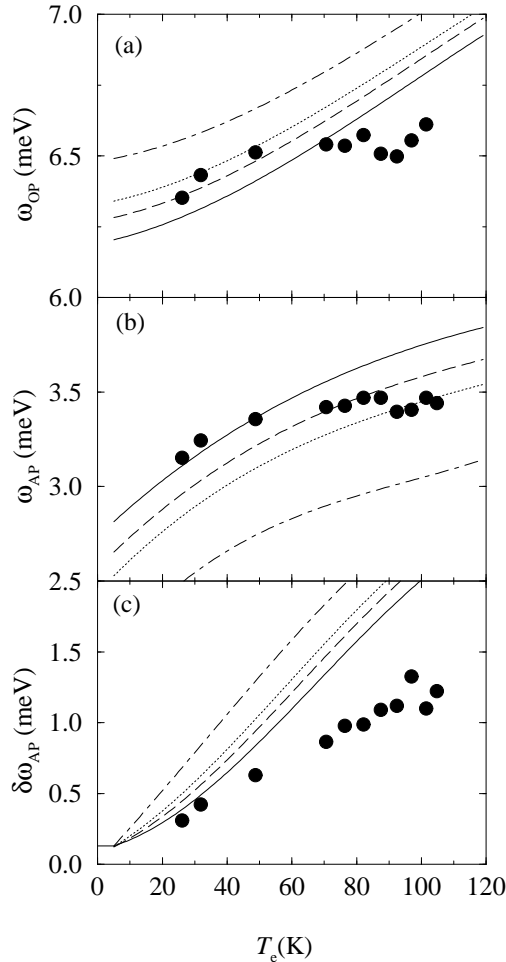


**Figure 15.** Experimental (●) and theoretical (curves) temperature ( $T_e$ ) dependences for  $q = 1.6 \times 10^5 \text{ cm}^{-1}$  of (a) the OP energy  $\omega_{\text{OP}}$ ; (b) the AP energy  $\omega_{\text{AP}}$ ; (c) the AP damping  $\delta\omega_{\text{AP}} \equiv (y_1 + y_2)$ . The theoretical curves have been determined within the RPA using a Hubbard local field correction for a total electron density  $N_1 + N_2 = 3.9 \times 10^{11} \text{ cm}^{-2}$  with  $N_1/N_2 = 1.0$  (solid lines), 1.9 (dashed lines), 2.3 (dotted lines) and 4.0 (dot-dashed lines).

calculated within the framework of a static theory) cannot explain our observed results. This is one of the central conclusions of this work.

We are led therefore to consider whether a complex local field correction,  $G_{11} = G'_{11} + iG''_{11}$ , as suggested in the context of a dynamic local field theory [14, 45], is any more successful in characterizing the observed behaviour. For a given temperature  $T_e$ ,  $G'_{11}$  (the real part of  $G_{11}$ ) was determined from the energy of the acoustic plasmon  $\omega_{\text{AP}}$ ;  $G''_{11}$  (the imaginary part of  $G_{11}$ ) was found to have a negligible affect on  $\omega_{\text{AP}}$ . Singwi and Tosi [8] have argued that the imaginary part of the local field correction is important in determining the lifetimes of plasmon modes. So, using the derived value for  $G'_{11}$ , the imaginary part  $G''_{11}$  was then determined by fitting the plasmon damping  $\delta\omega_{\text{AP}}$ . In order to give a reduction in the AP damping, to bring theory in line with experiment,  $G''_{11}$  was determined to be positive. As well as now providing complete agreement between experiment and theory for the  $T_e$ -dependence

of  $\omega_{\text{AP}}$  and  $\delta\omega_{\text{AP}}$ , the resulting complex local field factor,  $G_{11} = G'_{11} + iG''_{11}$ , was also found to provide a more accurate description of the optic plasmon energy  $\omega_{\text{OP}}$  and the AP asymmetry for both wavevectors  $q$  considered here. The variation with temperature  $T_e$  of these fitting parameters, the real and imaginary parts of  $G_{11}$ , is shown in figure 16 for the two wavevectors  $q$ . For  $T_e \lesssim T_F/2$ , the real and imaginary parts of the local field correction are similar to the values obtained within the STLS; in particular  $G''_{11}$  is zero. However, for  $T_e \gtrsim T_F/2$ , the temperature range over which the static STLS approach was found to fail, we see that both the real and imaginary parts of the intra-layer local fields increase with  $T_e$ . This is perhaps surprising, given our initial expectation that exchange–correlation effects should become less important with increasing temperature. Nevertheless, it is significant that the only way in which we have been able to obtain agreement between experiment and theory is through the incorporation of a complex local field correction.

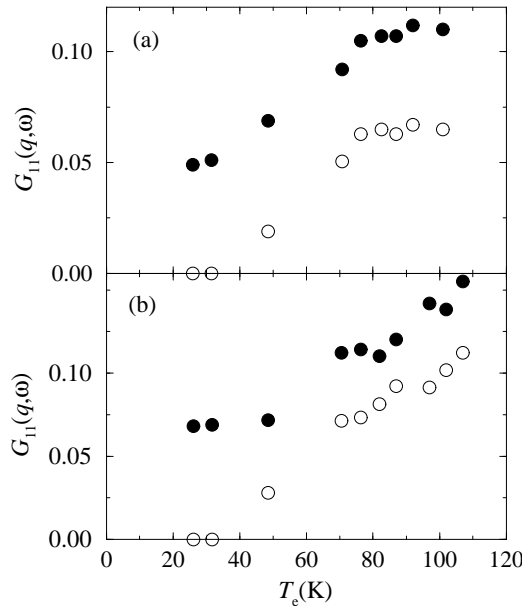


**Figure 16.** The temperature ( $T_e$ ) dependence of the real part  $G'_{11}$  (●) and imaginary part  $G''_{11}$  (○) of the intra-layer complex local field factor  $G_{11}(q, \omega)$ , used as a fitting parameter to provide agreement between experiment and theory for the AP energy  $\omega_{\text{AP}}$  and the AP damping  $\delta\omega_{\text{AP}}$ . The inter-layer local field factor is set to  $G_{12} = 0$  (a valid approximation given its relatively small magnitude). (a)  $q = 1.16 \times 10^5 \text{ cm}^{-1}$ , (b)  $q = 1.6 \times 10^5 \text{ cm}^{-1}$ .

Finally, we observe that our conclusions are consistent with the results of measurements of the AP-mediated Coulomb drag between two electron layers in samples similar to that studied here [24, 25]. In particular, in such experiments the onset temperature for plasmon enhancement of the drag rate is determined by the energies of the acoustic plasmons. A suppression of the AP energies from that expected within the RPA, as observed in our Raman measurements, should lead to the plasmon enhancement in the Coulomb drag rate occurring at a lower temperature than that predicted by the RPA; this is indeed observed in references [24] and [25]. On the other hand, an increase in the damping of the plasmons leads to an increase in the magnitude of the plasmon enhancement in the drag rate. Hill *et al* found that although the use of a Hubbard static local field factor resulted in better agreement between theory and experiment for the onset temperature, due to the suppression of the AP energies, the

resultant increase in the plasmon damping leads to an overestimate of the magnitude of the enhancement [24], which mirrors the results of the Raman measurements of the AP damping presented here (i.e. at higher temperatures we find that the plasmon damping is reduced from that predicted by theory). Our use of a complex local field factor to reconcile the behaviour of the plasmon energy and damping is consistent with the conclusions of Noh *et al.*, who suggested that a dynamic local field theory could account for their Coulomb drag results [25], although they implied that this would lead to a broadening of the plasmon modes, whereas we find the damping (as determined from the Raman lineshape) to be less than that predicted by the RPA.

## 7. Summary

To conclude, we have analysed the temperature dependence of the Landau damping of the acoustic plasmon in an electron bilayer, with a view to obtaining a measure of the importance of exchange–correlation effects in such systems. To this end, we have modelled the density response of our system using the Singwi–Tosi–Land–Sjölander (STLS) approximation, in which we have taken full account of the effects of finite temperature. The most significant message of these calculations is that non-zero temperature correlations within the STLS differ little from their zero-temperature counterparts at low wavevector. Increasing the temperature leads to an increase in the kinetic energy of the electron gas, implying a decrease in the significance of many-body effects in determining its behaviour. Naïvely we could have expected our temperature-dependent local field corrections to show a transition from the H-RPA (a model including exchange–correlation effects to some degree) to the RPA (a model in which exchange and correlation are not included) [20]. If this were the case we would have expected a much greater decline in the local field corrections towards zero as  $T_e$  is increased. However, this does not seem to be the case for the static local field corrections that we have calculated within the STLS.

Experimentally, we determined the electron temperature of the 2DEGs from measurements of the photoluminescence, which gives an accurate determination of the temperature under the same conditions as for the Raman measurements. Our Raman lineshapes displayed the clear signature of Landau damping of the acoustic plasmon, indicated by the asymmetric form of the Raman peak. Careful analysis of the spectra allowed us to extract three parameters which characterize the lineshape and energy of the acoustic plasmon:  $y_1$  and  $y_2$ , the low- and high-Raman-shift halfwidths of the plasmons, and the AP energy itself. These parameters were compared with theoretically calculated values, determined within the RPA and within the H-RPA and STLS local field theories, thereby giving us a means to analyse the success of these theories in modelling electron gases of intermediate degeneracy. We found that for  $T_e \lesssim T_F/2$  the inclusion of exchange–correlation effects using a local field correction is necessary—indeed sufficient—to obtain good quantitative agreement for the asymmetric Landau damping. Conversely, for  $T_e \gtrsim T_F/2$  none of the theories modelled successfully the AP asymmetry, or its upward shift in energy with increasing  $T_e$ . Further, the behaviour of the AP energy and damping cannot be reconciled to the calculations by a reduction with  $T_e$  of the 2DEG density, or a redistribution of electrons between the two quantum wells. This leaves only exchange–correlation effects as the cause of the discrepancy between experiment and theory. We find that the STLS approach and indeed any static local field theory cannot effectively model the exchange–correlation effects apparent in the experimental data.

We should note also that we observed a greater discrepancy between experiment and theory for a wavevector of  $q \sim 0.1k_F$  than for  $q \sim 0.14k_F$ . Indeed, for the lower wavevector the Landau damping of the AP appeared to be effectively constant over the whole temperature range considered.

There are a number of alternative, although less widely applied, theoretical approaches to that of the STLS. It may be that a non-local scheme (see, e.g., references [11] and [12]) may be necessary for a true description of the excitation spectra of low-dimensional electron systems. However, from our work the most promising candidate is probably a quantum STLS approach, employing a frequency-dependent local field correction [14, 46], which may go towards providing a more complete agreement between experiment and theory; we have shown that we are able to obtain excellent agreement between experiment and theory using as a fitting parameter a complex local field factor, as suggested in the context of a dynamical local field theory. Our work shows that the temperature dependence of Landau damping is likely to be a valuable experimental probe of these theories.

### Acknowledgments

We thank the UK Engineering and Physical Sciences Research Council, the Royal Society, and the UK Defence Evaluation and Research Agency for support. We are grateful to K Zolleis for the Shubnikov-de Haas measurements and to CHW Barnes for numerical assistance.

### Appendix A

We describe here our implementation of the STLS scheme for electron bilayers. The density response functions  $\chi_{ij}(q, \omega)$  will have poles on (or infinitesimally close to) the real  $\omega$ -axis which correspond physically to the energies of the plasmon modes, while the poles of the coth function in equation (13) will lie equispaced along the imaginary  $\omega$ -axis. A Wick rotation ( $\omega \rightarrow i\omega$ ) allows us to evaluate the integral for the static structure factors  $S_{ij}(q)$  in equation (13) as a contour integral along the imaginary  $\omega$ -axis, where the poles of the integrand are now just the poles ( $\gamma_\nu = 2\pi i\nu k_B T/\hbar$ ,  $\nu = 0, \pm 1, \pm 2, \dots$ ) of  $\coth(\hbar\omega/2k_B T)$ . The residue theorem then allows a transformation of the integral into a sum over imaginary (Matsubara) frequencies giving

$$S_{ij}(q) = -\frac{k_B T}{\sqrt{N_i N_j}} \sum_{\nu=-\infty}^{\nu=\infty} \chi_{ij}(q, \gamma_\nu). \quad (\text{A.1})$$

For convenience, we now assume that the two layers are of equal density, i.e.  $N_i = N_j = N$ . Defining  $\Phi_{ij}(q, \gamma_\nu) = -(E_F/N)\chi_{ij}(q, \gamma_\nu)$ , we have

$$S_{ij}(q) = \sum_{\nu=-\infty}^{\nu=\infty} \Phi_{ij}(q, \gamma_\nu) \theta \quad (\text{A.2})$$

where  $\theta = k_B T/E_F = T/T_F$  and  $E_F$  and  $T_F$  are the Fermi energy and temperature. From equation (2) we have

$$\overline{\overline{\Phi}} = \frac{\Phi_1}{1 - \tilde{v}_{12}^2 \Phi_1^2} \begin{pmatrix} 1 & -\tilde{v}_{12} \Phi_1 \\ -\tilde{v}_{12} \Phi_1 & 1 \end{pmatrix} \quad (\text{A.3})$$

$$\Phi_1 = \frac{\Phi_{2D}^0}{1 + \Phi_{2D}^0 \tilde{v}_{11}}. \quad (\text{A.4})$$

$\Phi_{2D}^0$  has been evaluated explicitly by Phatisena *et al* who derived the form [47]

$$\Phi_{2D}^0(q, \gamma_\nu) = \int_0^\infty k f(k) \frac{|2 \cos(\phi)|}{[(q^4/4 - k^2 q^2 - \gamma_\nu^2) + q^4 \gamma_\nu^2]^{1/4}} dk \quad (\text{A.5})$$

where  $f(k)$  is the Fermi–Dirac distribution function and

$$\tan(2\phi) = \frac{q^2 \gamma_v^2}{q^4/4 - k^2 q^2 - \gamma_v^2}. \quad (\text{A.6})$$

Note that in the case of a negative denominator,  $2\phi$  has to be replaced by  $\pi - 2\phi$ .

Thus in order to evaluate  $S_{ij}(q)$  we must evaluate equation (A.2) using equation (A.3).  $S_{11}(q)$  can be written as

$$S_{11}(q) = \sum_{v=-\infty}^{\infty} \frac{\theta \Phi_1(q, \gamma_v)}{1 - \tilde{v}_{12}^2(q) \Phi_1^2(q, \gamma_v)} \quad (\text{A.7})$$

which is reformulated as

$$S_{11}(q) = \underbrace{\sum_{v=-\infty}^{\infty} \theta \Phi_1(q, \gamma_v)}_{S_{2D}(q)} + \underbrace{\sum_{v=-\infty}^{\infty} \frac{\theta \tilde{v}_{12}^2(q) \Phi_1^3(q, \gamma_v)}{1 - \tilde{v}_{12}^2(q) \Phi_1^2(q, \gamma_v)}}_{\Delta S}. \quad (\text{A.8})$$

The first term in equation (A.8) is the structure factor for a single-electron layer,  $S_{2D}(q)$ . The second, inter-layer term  $\Delta S$  is  $O(\Phi_1^3)$  and acts as a (small) perturbation, reflecting the small extent to which the second layer affects intra-layer correlations.

$S_{12}(q)$  is given by

$$S_{12}(q) = - \sum_{v=-\infty}^{\infty} \frac{\theta \tilde{v}_{12}^2(q) \Phi_1^2(q, \gamma_v)}{1 - \tilde{v}_{12}^2(q) \Phi_1^2(q, \gamma_v)} \quad (\text{A.9})$$

which is  $O(\Phi_1^2)$  and hence again generally acts as a perturbation. The explicit evaluation of the sums to calculate  $S_{11}(q)$  and  $S_{12}(q)$  is performed in an analogous manner to the single-layer case, as described by Schweng and Bohm [39].

We can note in passing that the success of the relatively simple H-RPA approach when applied to bilayer systems can be traced directly to equations (A.8) and (A.9): the H-RPA includes quite effectively the  $O(\Phi_1)$  contribution to the local field in a bilayer system. The STLS formalism, however, includes the inter-layer exchange and correlation, and the perturbation of the intra-layer correlations by the presence of the second layer.

We can rewrite equation (15) for the local field factors  $G_{ij}(q)$  for the case of equal densities in terms of dimensionless variables ( $\mathbf{Q} = \mathbf{q}/k_F$ ,  $\mathbf{K} = \mathbf{k}/k_F$ ) as

$$G_{ij}(\mathbf{Q}) = \frac{1}{2\pi} \int d\mathbf{K} \frac{\mathbf{Q} \cdot \mathbf{K}}{|\mathbf{Q}| |\mathbf{K}|} \frac{F'_{ij}(|\mathbf{K}|)}{F'_{ij}(|\mathbf{Q}|)} [\delta_{ij} - S'_{ij}(|\mathbf{Q} - \mathbf{K}|)] \quad (\text{A.10})$$

where  $S'_{ij}(|\mathbf{Q} - \mathbf{K}|) = S_{ij}(|\mathbf{q} - \mathbf{k}|)$  and  $F'_{ij}(|\mathbf{Q}|) = F_{ij}(|\mathbf{q}|)$ . Following Jonson in using the substitution  $\mathbf{C} = \mathbf{Q} - \mathbf{K}$ , and with  $a = C/Q$ , we have as our final form [1]

$$\begin{aligned} G_{ij}(\mathbf{Q}) &= \frac{1}{2\pi} \int_0^\infty dC C [\delta_{ij} - S'_{ij}(C)] \\ &\times \int_0^{2\pi} d\mathbf{Q} \frac{F'_{ij}(|\mathbf{Q}| \sqrt{1 + a^2 + 2a \cos \phi})}{F'_{ij}(|\mathbf{Q}|)} \frac{a \cos \phi}{\sqrt{1 + a^2 + 2a \cos \phi}}. \end{aligned} \quad (\text{A.11})$$

Equations (A.2), (A.3) and (A.11) were solved self-consistently using a method due originally to Ng to accelerate (ensure) convergence [48]. For low number densities (i.e.  $r_s \geq 2$ ) it was also found that the initial value of  $G_{11}(q)$  has to be chosen carefully in order to ensure convergence; parametrized forms given in reference [49] were used as the initial seeds.

## References

- [1] Jonson M 1976 *J. Phys. C: Solid State Phys.* **9** 3055
- [2] Gold A 1992 *Z. Phys. B* **86** 193
- [3] Neilson D, Swierkowski L, Szymanski J and Liu L 1993 *Phys. Rev. Lett.* **67** 4035
- [4] Zheng L and Macdonald A H 1994 *Phys. Rev. B* **49** 5522
- [5] Liu L, Swierkowski L, Neilson D and Szymanski J 1996 *Phys. Rev. B* **53** 7923
- [6] Hubbard J 1957 *Proc. R. Soc. A* **243** 336
- [7] Singwi K S, Tosi M P, Land R H and Sjölander A 1968 *Phys. Rev.* **176** 589
- [8] Singwi K S and Tosi M P 1981 *Solid State Physics* vol 36 (New York: Academic) p 177
- [9] Mahan G D 1981 *Many Particle Physics* (New York: Plenum)
- [10] Ceperley D M and Alder B J 1980 *Phys. Rev. Lett.* **45** 566  
Tanatar B and Ceperley D M 1989 *Phys. Rev. B* **39** 5005
- [11] Ryan J C 1991 *Phys. Rev. B* **43** 12 406
- [12] Luo M S-C, Chang S L, Schmitt-Rink S and Pinczuk A 1993 *Phys. Rev. B* **48** 11 086
- [13] Kalman G and Golden K I 1998 *Phys. Rev. B* **57** 8834
- [14] Moudgil R K, Ahluwalia P K and Pathak K N 1995 *Phys. Rev. B* **52** 11 945
- [15] Larson B C, Tischler J Z, Isaacs E D, Zschack P, Fleszar A and Eguiluz A G 1996 *Phys. Rev. Lett.* **77** 1346
- [16] Das Sarma S and Madhukar A 1981 *Phys. Rev. B* **23** 805
- [17] Abstreiter G, Cardona M and Pinczuk A 1984 *Light Scattering in Solids IV* ed M Cardona and G Güntherodt (Heidelberg: Springer) p 5
- [18] Pinczuk A and Abstreiter G 1988 *Light Scattering in Solids V* ed M Cardona and G Güntherodt (Heidelberg: Springer) p 153
- [19] Gammon D, Shanabrook B V, Ryan J C, Katzer D S and Yang M J 1992 *Phys. Rev. Lett.* **68** 1884
- [20] Kainth D S, Richards D, Hughes H P, Simmons M Y and Ritchie D A 1998 *Phys. Rev. B* **57** R2065
- [21] Kainth D S, Richards D, Bhatti A S, Hughes H P, Simmons M Y, Linfield E F and Ritchie D A 1999 *Phys. Rev. B* **59** 2095
- [22] Zettler T, Peters C, Kotthaus J P and Ploog K 1989 *Phys. Rev. B* **39** 3931
- [23] Allen B 1997 *MPh Thesis* University of Cambridge
- [24] Hill N P R, Nicholls J T, Linfield E H, Pepper M, Ritchie D A, Jones G A C, Hu B Y-K and Flensberg K 1997 *Phys. Rev. Lett.* **78** 2204
- [25] Noh H, Zelakiewicz S, Feng X G, Gramila T J, Pfeiffer L N and West K W 1998 *Phys. Rev. B* **58** 12 621
- [26] Flensberg K and Hu B Y-K 1994 *Phys. Rev. Lett.* **73** 3572
- [27] Flensberg K and Hu B Y-K 1995 *Phys. Rev. B* **52** 14 761
- [28] Stern F 1967 *Phys. Rev. Lett.* **18** 546
- [29] Fasol G, King-Smith R D, Richards D, Ekenberg U, Mestres N and Ploog K 1989 *Phys. Rev. B* **39** 12 695
- [30] Richards D, Fasol G and Ploog K 1990 *Appl. Phys. Lett.* **56** 1649
- [31] Vitilina R Z and Chaplik A V 1981 *Sov. Phys.-JETP* **54** 536
- [32] Jain J K and Das Sarma S 1987 *Phys. Rev. B* **36** 5949
- [33] Santoro G E and Giuliani G F 1988 *Phys. Rev. B* **37** 937
- [34] Mermin N D 1970 *Phys. Rev. B* **1** 2362
- [35] Maldague P F 1978 *Surf. Sci.* **73** 296
- [36] Hu G and O Connell R 1988 *J. Phys. C: Solid State Phys.* **21** 4325
- [37] Szymanski J, Swierkowski L and Neilson D 1994 *Phys. Rev. B* **50** 11 002
- [38] Tanaka S and Ichimaru S 1986 *J. Phys. Soc. Japan* **55** 2278
- [39] Schweng H K and Bohm H M 1994 *Z. Phys. B* **481**
- [40] Richards D, Wagner J and Schmitz J 1996 *Solid State Commun.* **100** 7
- [41] Madelung O 1996 *Semiconductors—Basic Data* (Berlin: Springer)
- [42] Coleridge P T 1991 *Phys. Rev. B* **44** 3793
- [43] Dobryakov S N and Lebedev Y S 1969 *Sov. Phys.-Dokl.* **13** 873
- [44] Krall N A and Trivelpiece A W 1973 *Principles of Plasma Physics* (New York: McGraw-Hill)
- [45] Richardson C F and Ashcroft N W 1994 *Phys. Rev. B* **50** 8170
- [46] Schweng H K and Bohm H M 1993 *Phys. Rev. B* **48** 2037
- [47] Phatisena S, Amritkar R E and Panat P V 1986 *Phys. Rev. A* **34** 5070
- [48] Ng K 1974 *J. Chem. Phys.* **61** 2680
- [49] Bulutay C and Tomak M 1996 *Phys. Rev. B* **54** 14 643